Design of fin structures for phase change material (PCM) melting process in rectangular cavities

DESIGN OF FIN STRUCTURES FOR PHASE CHANGE MATERIAL (PCM) MELTING PROCESS IN RECTANGULAR CAVITIES

Rejane De Césaro Oliveski [1], Fábio Becker[1], Luiz Alberto Oliveira Rocha [1], Cesare Biserni [2] and Gabriel Eduardo Strohm Eberhardt[1]

1 Mechanical Engineering Graduate Program, Universidade do Vale do Rio dos Sinos, 93022-750 São Leopoldo, Brazil

[2] Dipartimento di Ingegneria Industriale, Università degli Studi di Bologna, Viale Risorgimento 2, 40136 Bologna, Italy

Abstract

The objective of this work is to analyze the lauric acid PCM melting process in a finned rectangular cavity, keeping both the PCM mass and the total fin area constant, thus changing only the fin aspect ratio. The analysis was conducted through a parametric study of 78 different fin configurations. In order to maintain the thermal capacity, the cavity and fin areas were kept constant while fin dimensions were varied within a preset number of combinations of area fraction and width. The fins tested were combinations of 9 fin aspect ratios (RA_f) and 9 fin-to-cavity area fractions (ϕ). A finite-volume numerical CFD method was used to obtain the results. Governing equations were the conservation of mass, momentum and energy while phase change was governed by an enthalpy-porosity model. The mathematical model was validated against reference experimental results and computational meshes were checked with GCI. For all tested cases, with an increase in the fin length and a consequent reduction in RA_f, there was a reduction of the total time of the melting process. The RA_f, which had shorter melting times, were defined as optimal aspect ratios (RA_{opt}). Thus, each ϕ tested resulted in its own RA_{opt}. For ϕ = 0.005, 0.01, 0.02, 0.03, 0.04, 0.05, 0.1, 0.2 and 0.3, RA_{opt} = 0.013, 0.026, 0.052, 0.078, 0.104, 0.130, 0.260, 0.592 and 0.889, respectively. Future works could contemplate a greater number of fins, with the same total area of this study, other PCM and other temperature differences, for example.

Keywords: Phase Change Material (PCM). Melting process. Numerical simulation. Fin aspect ratio, area fraction.

Nomenclature

A_c	cavity area, $A_c = H\ W$	[m^2]
A_f	fin area, $A_f = H_f / W_f$	[m^2]
C	porous zone constant	[kg m^{-3} s^{-1}]
c_p	specific heat	[J kg^{-1} K^{-1}]
Fo	Fourier number, $Fo = \alpha\ t / L_c^2$	[-]
$\vec{g}$	gravity	[m s^{-2}]
H	cavity height	[mm]
h	heat transfer coefficient	[W m^{-2} K]

k	thermal conductivity	[W m^{-1} K^{-1}]
L	latent heat	[J kg^{-1}]
L_c	characteristic length, $\left(L_c = A_c^{1/2}\right)$	[mm]
Nu	Nusselt number, $Nu = h\,L_c / k$	[-]
p	pressure	[Pa]
q''	heat flux	[W m^{-2}]
RA	aspect ratio, $AR = H / W$	[-]
$\vec{S}$	momentum equation source term	[Pa m^{-1}]
T	temperature	[K]
t	time	[s]
$\vec{V}$	velocity vector	[m s^{-1}]
W	cavity width	[mm]
W_f	fin width	[mm]

Greek symbols

β	liquid fraction	[-]
ε	computational constant	[0,001]
λ	specific enthalpy	[J kg^{-1}]
μ	dynamic viscosity	[kg m^{-1} s^{-1}]
ρ	density	[kg m^{-3}]
ϕ	area fraction, $\phi = A_f / A_c$	[-]

Subscripts

c	cavity
f	fin
i	initial
L	phase change
l	liquid
m	melting
opt	optimal
ref	reference

s	solid
se	sensible
w	wall

1. INTRODUCTION

The increase in energy demand, air pollution, energy prices, partial unavailability of fossil fuels and environmental concerns are driving causes of studies on alternative methods of energy production (Reddy, Mudgal, and Mallick 2018). As an extension, the development and application of energy storage techniques has become a crucial part of this area. Among the different forms of energy storage, thermal storage through sensible, latent or thermochemical heat (Zhang et al. 2016) has become one of the most used in several applications (Hasnain 1998; Dabiri, Mehrpooya and Nezhad 2018; Zhu, Ma, and Wang 2009). The latent heat technique has become more attractive due to its high energy storage capacity and the ability to provide heat at a constant temperature equal to the material transition temperature. The materials used in latent heat energy storage are called Phase Change Materials (PCM) (Ibrahim et al. 2017). These are classified according to their chemical composition into organic (paraffin and non-paraffin), inorganic (salt and metal hydrates), and eutectic (metal alloys) (Jamil et al., 2019, Ibrahim et al., 2017). As for the phase change temperature classification, three groups are universally accepted: low, medium, and high temperature, Ehms et al., 2019. According to Pielichowska et al., (2014), PCM is considered low temperature when the phase change occurs at up to 15 °C, medium temperature when the phase change should occur between 15 °C and 90 °C, and high temperature when the phase change occurs above 90 °C.

The selection of a PCM depends on its thermal properties, applications, stability and cost (Aslfattahi et al., 2020). Their application can occur in many areas such as biomedicine, textile, automotive (Jaguemont et al., 2018) and construction (Pielichowska and Pielichowski 2014, Souayfane et al. 2016), solar power plants (Zhang et al. 2016, Khan et al. 2017) and electronic components (Baby e Balaji 2012, Kalbasi and Salimpour, 2015). In buildings, PCM can be used for cooling in passive or active systems (Souayfane et al. 2016). For example, one way of using PCM in buildings is through the inclusion of micro-encapsuleted PCM in the materials used in construction (Kalnaes et al., 2015). Another interesting application of PCM is in the temperature control of electric car batteries. In this case, according to Jaguemont et al. (2018), PCM should have a melting point between 45 °C and 50 °C to obtain greater efficiency. Solar absorption refrigeration systems can also use PCM adapted to the working temperature, mass rate and loading and unloading time (Khan et al. 2017). Another interesting application refers to the use of PCM as thermal protection for food

products sensitive to thermal variations (Leducq et al. 2015). In terms of cooling electronic components, Baby e Balaji (2012) studied experimentally the application of PCM with different types of fins and at different power levels. It was found that, by including PCM in the finned cavity, the electronic device showed a significant improvement in operating time.

PCMs have several advantages: small volumetric variation during phase change processes, high specific heat and latent melting heat (Baby and Balaji 2012) as well as thermal stability (Jaguemont et al. 2018). On the other hand, these materials have characteristic low thermal conductivities which result in low charge and discharge rates (Akeiber et al. 2016; Pizzolato et al. 2017). Therefore, it is necessary to incorporate additional techniques to improve heat transfer between the cavity and PCM. Among these techniques there are: multiple PCM usage (Ibrahim et al. 2017), high thermal conductivity particle dispersion in the PCM (Wu et al. 2020), microencapsulation (Sun et al. 2019) and fins. According to Kean et al. (2018), the inclusion of nanoparticles can reduce the time of the melting or solidification processes. But, if nanoparticle concentration is in excess, a negative effect may occur due to the agglomeration of material. In terms of thermal and enthalpic stability with nanoparticle PCM, Aslfattahi et al. (2019) found an increase in thermal stability as well as a decrease in melting point, compared to pure material.

Baby and Balaji (2012) studied experimentally the application of PCM to cool electronic components. Different types of fins were investigated at different power levels. It was found that, by including PCM in the finned cavity, the electronic device showed a significant improvement in operating time. In general, fins result in an increase in active area and promote natural convection and associated thermal processes such as phase change. Consequently, the natural convection process is a defining parameter in the efficiency of finned systems. Fin geometry and positioning are also important to the phase change process (Kazemi et al. 2018; Pu et al. 2020; Abdulateef et al. 2017). In tubular systems, longitudinal fins placed at the bottom of the cavity allowed the formation of recirculation zones which decreased PCM melting time (Kazemi et al. 2018). In comparison, tubular systems with radial fins were also studied with variations in height and number of fins while keeping the volume fraction and thickness constant (Pu et al. 2020). In this case it was determined that configurations with longer fins decreased natural convection, reduced fin interactions and increased melting time but an intermediate length was deemed the most adequate. Triple tube cavities were studied with different configurations of rectangular and triangular fins (Abdulateef et al. 2017). Results showed that placement of the fins affected substantially natural convection and could reduce total melting times.

Several different fin geometric characteristics can be varied to evaluate their effect in PCM melting. In the case of varying fin thickness in rectangular cavities, an optimum ratio of fin thickness to combined fin + PCM volume which increased heat transfer rate through the fin but did not reduce considerably heat transferred from the wall to the PCM was determined (Mostafavi, Parhizi, and Jain 2019). Fin thickness was also found to be directly proportional to heat transfer through it and inversely proportional to temperature at its base, which improved cooling in the system (Arshad et al. 2020). Fins of different geometries were also examined in the melting process of paraffin PCM with or without nanoparticles (Kok 2020). In this case, fin geometries that probed into regions of un-melted PCM resulted in more satisfactory results than conventional fins despite having less heat transfer surface area. Melting lauric acid PCM was studied in rectangular cavities with 3 fins of different widths and placement (Joshi and Rathod 2019). It was determined that reducing the width of upper fins did not affect melting time but increased thermal storage capacity. Melting RT42 PCM was studied numerically in rectangular cavities with two fins with varying lengths placed at different heights while maintaining a constant total length (Ji et. al., 2018). It was proven that placement of shorter fins higher and longer fins lower reduced total melting time when compared to two fins of equal length. However, there was a limit to the length of the shorter fin, below which there were no changes to melting time. Of these, fins are the most attractive due to ease of construction and low manufacturing cost (Agyenim et al. 2010).

There are several studies in the literature on PCM melting/solidification in finned cavities. However, studies of this type that maintain constant total fin area and PCM mass have not been found in the literature. Thus, the objective of this study is to analyze the PCM melting process in a finned rectangular cavity keeping both the PCM mass and the total fin area constant, thus changing only the fin aspect ratio. With this, it becomes possible to determine the optimal aspect ratio to minimize the total melting time for different fractions of the area between fin and cavity.

2.1 Physical Domain

The studied physical domain, depicted in Fig. 1, consisted of a two-dimensional rectangular cavity with a width (W) of 50 mm and height (H) of 120 mm filled with lauric acid PCM initially in a solid-state. A “negative fin”, i.e. a morphing lateral intrusion, was positioned horizontally at the center of the right wall with specified width (W_f) and height (H_f). A 2 mm opening was located in the upper wall near the right side to simulate the loss of PCM from the cavity during the melting process. While classical fin problems with a fixed temperature at its base do result in variations of temperature

along the length of the fin, the physical scale of the problem results in essentially a constant-temperature fin. This was observed in the experimental study of Kamkari and Shokouhmand 2014; and used to validate the numerical results of Joshi and Rathod 2019. So, it also was incorporated as a boundary condition in this work. The upper, lower, left side, front and rear walls were considered thermally insulated. This condition guaranteed null heat flow through these walls. Furthermore, with this condition, there was no temperature difference between the front and rear walls. Consequently, no considerable flow or circulation was expected to develop along this direction and the physical problem can be considered two-dimensional.

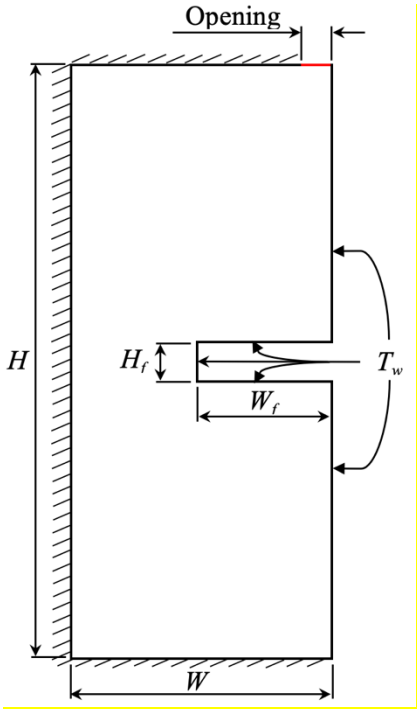

Figure 1 – 2D cavity domain with a morphing lateral intrusion shaped as a fin.

The constraints of the parametric study were the cavity area ($A_c = HW$) and the fin area ($A_f = H_f W_f$). Area A_c was kept constant and equal to 6,000 mm^2 while A_f was obtained from the area fraction $\left(\emptyset = A_f/A_c\right)$. Nine values of ϕ (0.005, 0.01, 0.02, 0.03, 0.04, 0.05, 0.1, 0.2 and 0.3) as well as nine values of W_f (10 mm, 15 mm, 20 mm, 25 mm, 30 mm, 35 mm, 40 mm, 45 mm and 48 mm) were selected. Through combinations of A_c, ϕ, and W_f, values of A_f and H_f were obtained and it was possible to calculate the fin aspect ratio $\left(RA_f = H_f/W_f\right)$. The selected values of ϕ and W_f resulted, ideally, in 81 geometric configurations. Of these, 3 of them could not be simulated as they exceeded the cavity dimensions and were discarded. Table 1 shows the dimensions of the remaining 78 fins.

Table 1 – Range of dimensions of fins tested.

		W_f [mm]								
		10	15	20	25	30	35	40	45	48
ϕ = 0.005		3.00	2.00	1.50	1.20	1.00	0.86	0.75	0.67	0.63
ϕ = 0.01		6.00	4.00	3.00	2.40	2.00	1.71	1.50	1.33	1.25
ϕ = 0.02		12.00	8.00	6.00	4.80	4.00	3.43	3.00	2.66	2.50
ϕ = 0.03		18.00	12.00	9.00	7.20	6.00	5.14	4.50	4.00	3.75
ϕ = 0.04	H_f [mm]	24.00	16.00	12.00	9.60	8.00	6.86	6.00	5.33	5.00
ϕ = 0.05		30.00	20.00	15.00	12.00	10.00	8.57	7.50	6.66	6.25
ϕ = 0.10		60.00	40.00	30.00	24.00	20.00	17.14	15.00	13.33	12.50
ϕ = 0.20			80.00	60.00	48.00	40.00	34.29	30.00	26.66	25.00
ϕ = 0.30				90.00	72.00	60.00	51.43	45.00	40.00	37.50

The properties of lauric acid are shown in Tab. 2, Tab. 3 and Tab. 4. Table 2 presents the values of specific heat (c_p), density (ρ), temperature (T), and latent heat (L).

Table 2 - Properties of lauric acid (Adapted of Kamkari and Shokouhmand 2014).

Specific heat capacity solid/liquid [J/(kg K)]	2,180/2,390
Density solid/liquid [kg/m^3]	940/885
Melting temperature range [K]	316.65/321.35
Latent heat [J/kg]	187,210

Thermal conductivity (k) and dynamic viscosity (μ) of lauric acid as a function of temperature were obtained by linear interpolation and are presented in Tab. 3 and 4, respectively. It is worth mentioning that regarding the nonmetallic PCMs, heat conduction mainly relies on the vibration of the crystal lattice, as addressed by Wu et al. (2020). The lattice component of thermal conductivity strongly depends on the way the molecules are arranged. More specifically, the temperature increase leads to a weakening of the atomic bonds, which in turn causes heat transfer inhibition. Thus, the mechanism mentioned above justifies the feeble reduction of thermal conductivity with the augmentation of temperature illustrated in Tab. 3.

Table 3 - Thermal conductivity of lauric acid (Shokouhmand and Kamkari 2013).

T [K]	293	303	313	323	328	333	338	343
k [W/(m K)]	0.161	0.159	0.158	0.145	0.143	0.142	0.139	0.138

Table 4 - Dynamic viscosity of lauric acid (Valeri and Meirelles 1997).

T [K]	321.2	322	333	344	355	372	383
μ [kg/(m s)]	0.00760	0.00747	0.00542	0.00428	0.00338	0.00250	0.00210

2.2 Mathematical Model

The mathematical model used to represent the melting process consisted of the equations of conservation of mass, momentum and energy shown in Eq. (1-3), respectively:

$$\frac{\partial \rho}{\partial t} + \nabla\left(\rho \vec{V}\right) = 0 \quad (1)$$

$$\frac{\partial}{\partial t}\left(\rho \vec{V}\right) + \nabla\left(\rho \vec{V}\vec{V}\right) = \nabla\left(\mu \nabla \vec{V}\right) - \nabla p + \rho \vec{g} + \vec{S} \quad (2)$$

$$\frac{\partial}{\partial t}\left(\rho\lambda\right) + \nabla\left(\rho \vec{V}\lambda\right) = \nabla\left(k \nabla T\right) \quad (3)$$

where $\vec{V}$ represents the velocity vector, t is the time, p is the pressure, $\vec{g}$ is the acceleration of gravity, $\vec{S}$ is the source term, and λ is the total enthalpy. The total enthalpy is obtained by adding the change in enthalpy associated with phase change (λ_L) and sensible enthalpy (λ_{se}), obtained through Eq. (4):

$$\lambda_{se} = \lambda_{ref} + \int_{T_{ref}}^{T} c_p dT \quad (4)$$

where λ_{ref} is the enthalpy at the reference temperature (T_{ref} = 298 K). The enthalpy in phase change is calculated as $\lambda_L = \beta L$.

For the PCM melting process, an enthalpy porosity model (Voller and Prakash 1987) was used. The model treated the solid-liquid interface zone (mushy zone) as a porous zone with the source term obtained from Eq. (5):

$$\vec{S} = \frac{(1-\beta)^2}{(\beta^3+\varepsilon)} C \vec{V} \quad (5)$$

where β is the liquid fraction, ε is a constant with value of 0.001 used to prevent division by zero and C is the porous zone constant. This constant depends on the morphology of the porous zone (Voller

and Prakash 1987). The net fraction of PCM within the phase change range is calculated from Eq. (6):

$$\beta = \begin{cases} 0 & se \quad T < T_S \\ 1 & se \quad T > T_l \\ T - T_S / T_l - T_S & se \quad T_S < T < T_l \end{cases} \tag{6}$$

The boundary conditions adopted were of adiabatic left, lower and upper walls of the domain, shown in Eq. (7-9), respectively:

$$-k \frac{\partial T}{\partial x}\Big|_{\substack{x=0 \\ y=0-H}} = 0 \tag{7}$$

$$-k \frac{\partial T}{\partial y}\Big|_{\substack{x=0-W \\ y=0}} = 0 \tag{8}$$

$$-k \frac{\partial T}{\partial y}\Big|_{\substack{x=W-opening \\ y=0}} = 0 \tag{9}$$

while a prescribed temperature condition was applied on the right vertical wall, all fin surfaces and the opening, as shown in Eq. (10, 11), respectively:

$$T|_{\substack{x=W \\ y=0-H}} = T_w \tag{10}$$

$$T|_{\substack{x=opening \\ y=H}} = T_a \tag{11}$$

3 Numerical Model

Numerical simulations were performed on ANSYS FLUENT® and the computational meshes were created on ANSYS ICEM® version 18.2. In the reference experimental work of Kamkari and Shokouhmand (2014), the liquid PCM was removed manually. In the present numerical work, this PCM removal was modeled through the "*pressure-outlet*" boundary condition imposed on the opening, with gauge pressure of 0 Pa and temperature of 343 K. For the pressure correction and pressure-velocity coupling, the "*presto*" and "*simple*" criteria were adopted, respectively. The flow was considered laminar transient with a time step of 0.1 s. In the energy and momentum equations, a "*first-order upwind*" scheme was used. Absolute convergence criteria of 10^{-8} for the energy equation and 10^{-5} for the velocity and continuity equations were adopted. Relaxation coefficients used were:

0.15 for pressure and momentum, 0.3 for density, field forces and energy and 0.2 for the liquid fraction. Intermediate values of k e μ were obtained by linear interpolation of the data of Tab. 3 and Tab. 4. The value of ρ_s was considered constant as of Tab. 2; however, values of ρ_l were pre-set from reference (Chuah et al. 2006) according to temperature: 885 kg/m^3 at 321.35 K (Tab. 1), 870 kg/m^3 at 323 K and 862 kg/m^3 at 333 K. The lower, upper, and left walls of the cavity were defined as adiabatic. The right wall and the fin surfaces were kept at the heating temperature T_w = 343 K. The no-slip condition was applied in all walls and the fin surfaces, except for the opening, which was considered free flow at T_a = 343K. In addition, the PCM was subjected to an initial temperature of T_i =298 K.

3.1 Model Validation and Mesh Test Sensitivity

3.1.1 Model Validation

Numerical validation was performed with comparisons to reference experimental data (Kamkari and Shokouhmand 2014) in two ways: through liquid fraction field and with the liquid fraction profile over time. The reference study consisted of the melting process of lauric acid PCM in a similar physical domain. The experimental rectangular cavity measured 50 mm in width, 120 mm in height and 120 mm in thickness, with a fin 25 mm in width and 4 mm in height. The fin and the right wall were subjected to a constant temperature of 343 K while the remaining walls were thermally insulated. The PCM was initially at a temperature of 298 K, i.e., solid-state (Kamkari and Shokouhmand 2014).

Figure 2 shows a comparison of liquid fraction fields (β) from the reference experimental study (Kamkari and Shokouhmand 2014) and the present numerical study at 10 min, 30 min and 50 min of the melting process. Figures 2(a, c, e) contain the experimental results and Figs. 2(b, d, f) the numerical results. In the numerical results, white and blue colors represent the solid-state PCM, while black and red colors represent the liquid state. As seen in Fig. 2, there is good visual agreement in the liquid fraction between both sets of results for all melting times.

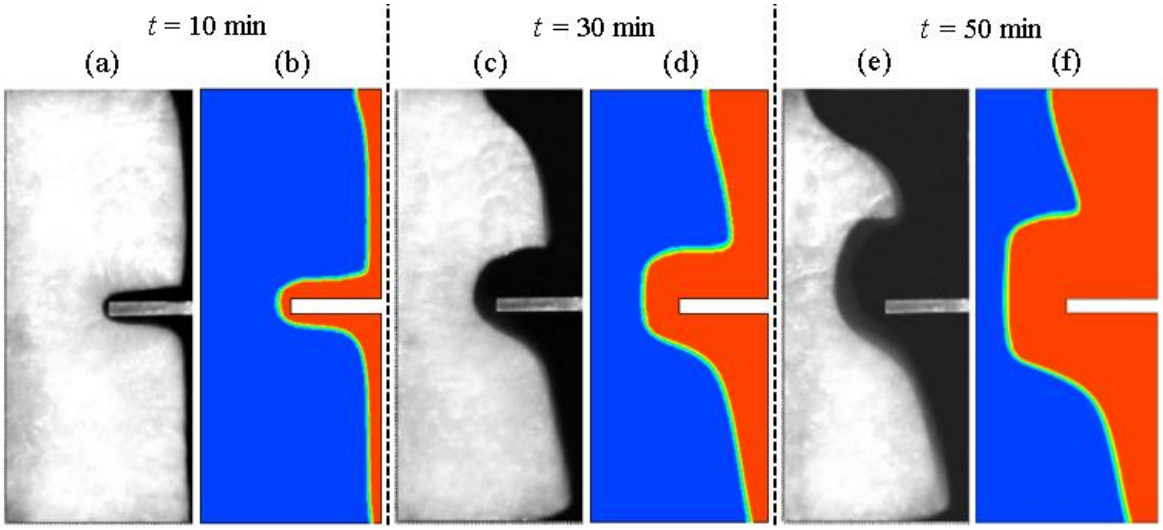

Figure 2 - β distribution at time t = 10 min, 30 min and 50 min: (a), (c) and (e) experimental results (Kamkari and Shokouhmand 2014); (b), (d) and (f) present numerical results.

Furthermore, Fig. 3 shows transient profiles of β obtained experimentally (Kamkari and Shokouhmand 2014) and numerically (present study). The values of β range from 0 to 1, with 0 representing the solid-state PCM and 1 representing the liquid state. Coherent agreement can be clearly observed between the numerical and experimental results. The average difference was approximately 5.4%, while the maximum difference was approximately 6.3% at t = 110 min with β = 0.856.

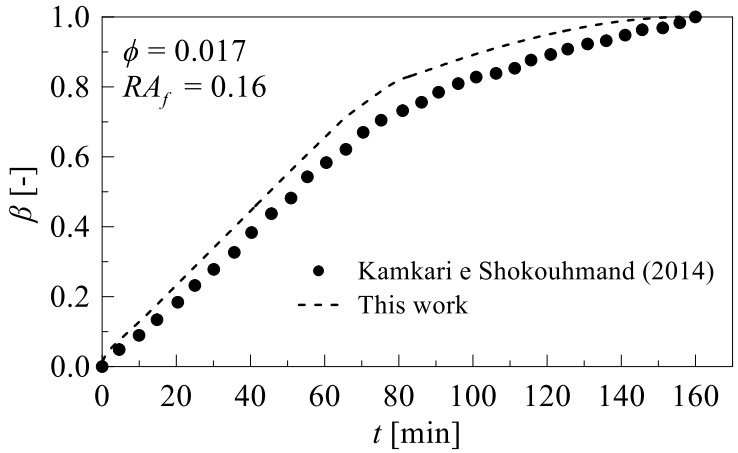

Figure 3 – Liquid fraction β as function of time t: comparison between experimental results (Kamkari and Shokouhmand 2014) and present numerical results.

Considering the good agreement between the numerical results of the present study and reference experimental results (Kamkari and Shokouhmand 2014), both qualitative (Fig. (2)) and

quantitative (Fig. (3)), as well as the constant value assigned to C (seen in Section 3.1.3), the numerical model used in this study was considered validated.

3.1.2 Mesh Test Sensitivity

For the present numerical study, three computational meshes were created, as seen in Fig. 4, with increasing number of elements. Meshes (a), (b) and (c) contained 10,118, 14,520 and 28,457 elements, respectively. Mesh independence analysis was performed using the GCI (Grid Convergence Method) procedure (Celik et al. 2008) by comparing the most refined mesh (c) with the intermediate mesh (b) and the least refined mesh (a). The calculated percentage rates were 1.9% and 5.5%, respectively. Thus, with a GCI of 1.9%, mesh (c) with 28,457 elements mesh was considered suitable for numerical simulations.

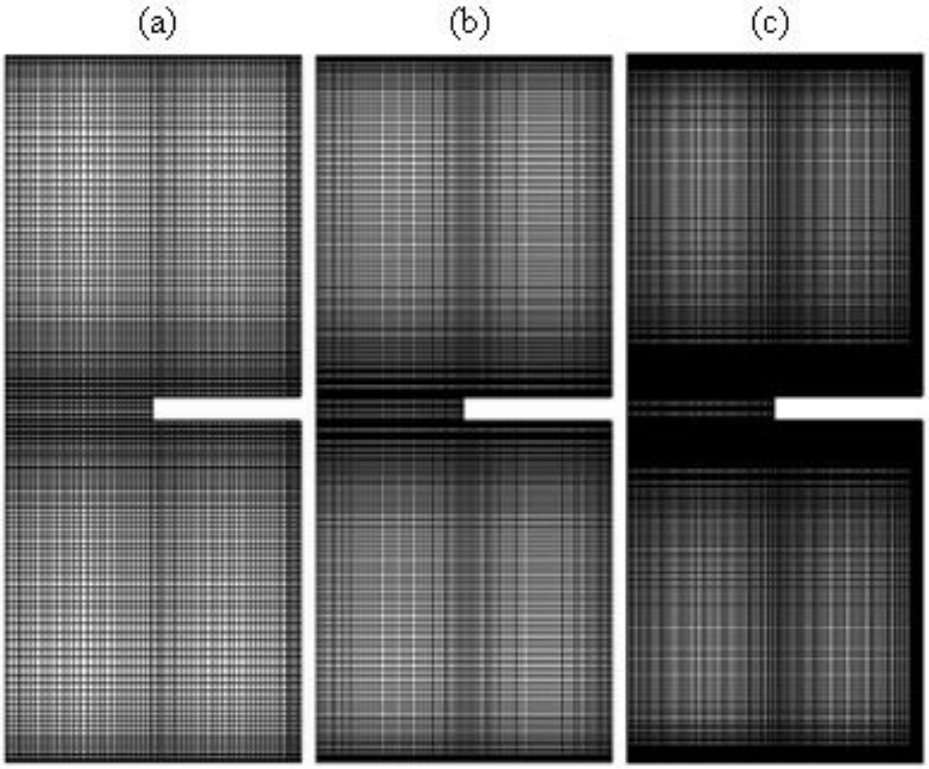

Figure 4 – Grid convergence study meshes: (a) 10,118, (b) 14,520 and (c) 28,457 elements.

3.1.3 Adjustment of porous zone constant "C"

The porous zone constant (C) of Eq. (5) indicated the material velocity damping to zero in the solid phase and its value had to be adjusted according to the problem analyzed. By definition, the value of C should be sufficient to allow flow in the transition region while at the same time

suppressing velocity in the solid phase (Voller and Prakash 1987). For the present study, a range of several orders of magnitude of C values were tested. It was observed that a value of C = 10^{11} more satisfactorily reproduced the PCM merging process and, consequently, was kept for all the numerical results presented in this study.

4. RESULTS AND DISCUSSIONS

The objective of this study was to analyze the influence of fin aspect ratio $\left(RA_f = H_f/W_f\right)$, and obtain the optimal aspect ratio (RA_{opt}), thereby minimizing the melting process time for each ϕ. For clarity, each parameter affecting optimization was analyzed individually.

4.1 Effects of Buoyancy on the Melting Process

Figures 5(a, b) show the velocity fields for RA_f = 0.288 and ϕ = 0.03 at times t = 20 min and 40 min, respectively. In the figures, PCM is represented with gray color in the solid phase and black color in the liquid phase, with the velocity field at the same instant of time superimposed. It can be seen in both figures that, due to the buoyancy force generated by the variation of temperature within the liquid phase, an upward flow is present close to the heated wall (right) and in the region above the fin. Downward flow can also be observed at the solid-liquid interface, thus ensuring the principle of mass conservation. In between these two convective currents and their velocity profile, it is possible to observe a shear region captured by the proper refinement of the computational mesh throughout the domain. Heating occurs along the upper side of the fin and beyond the reach of the vertical wall. In this region, a large recirculation zone is observed and can be classified as Rayleigh-Bénard convection. A similar flow can also be observed between the base of the cavity and the base of the fin, producing another recirculation zone in this region but with different characteristics.

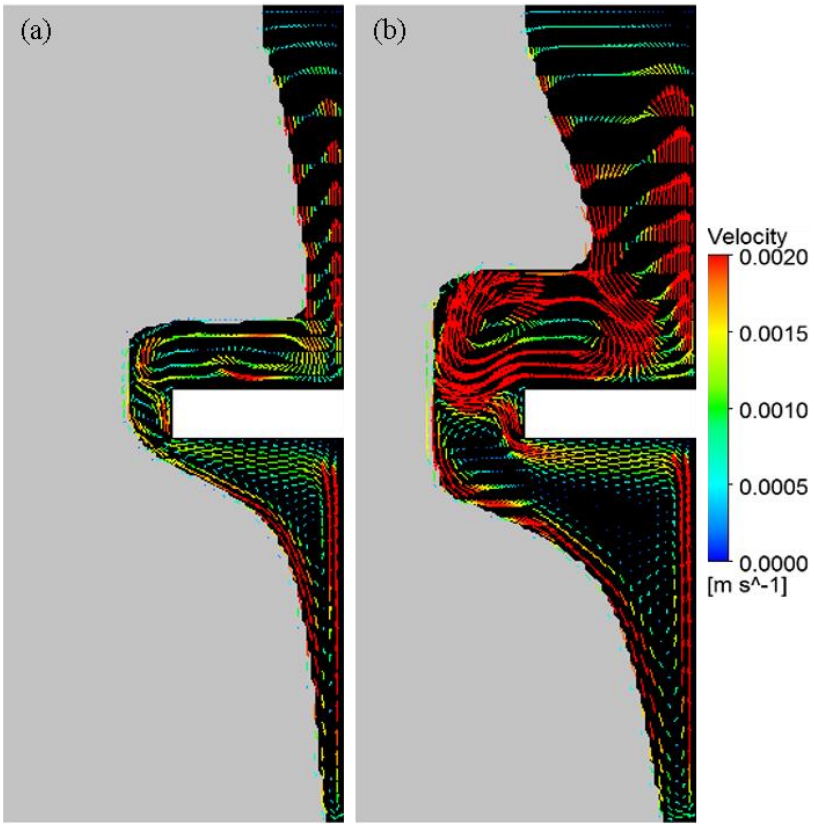

Figure 5 – Velocity distribution for RA_f = 0.288 and ϕ = 0.03 at: (a) t = 20 min, (b) t = 40 min.

Figures 6(a, b) show temperature fields for RA_f = 0.450 and 0.078 with ϕ = 0.03 at times t = 10 min and 50 min, respectively. In the figures, for all presented results, a robust thermal gradient near the right vertical wall and the entire perimeter of the fin can be initially observed. Strong thermal stratification is detected in the cavity at the final t = 50 min moment and especially in the region above and below the fin. Buoyant forces arising from the change in density near the active vertical wall form an upward convective current seen in Fig. 5(b). This current stratifies thermally the liquid PCM in the upper part of the cavity. A similar condition is observed below the fin for both tested values of RA_f, which contributes to the formation of a curved melting front. However, at t = 10 min and t = 50 min, there is an increase in thermal stratification in the region below the fin with decreasing RA_f. This behavior is related to the increase in fin perimeter, which limits the movement of the upward convective currents to the top of the cavity and contributes to accelerate the melting process. Slight temperature variations at the top of the fin at t = 10 min for both tested values of RA_f have also been detected. These characteristics fused layer instabilities are associated with Rayleigh-Bénard convection formation. Finally, it is worth mentioning that, for the others tested values of area fraction ϕ, this behavior is also observed.

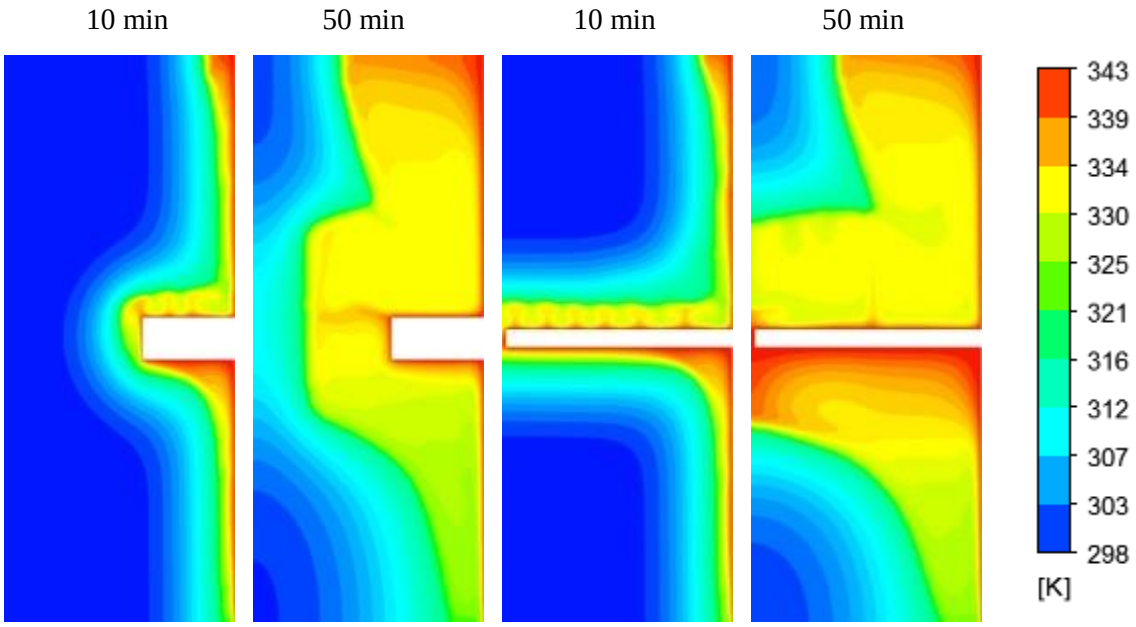

Figure 6 – Temperature distribution at t = 10 and 50 min, ϕ = 0.03 and: (a) RA_f = 0.450 and (b) RA_f = 0.078.

4.2 Area Fraction Effect

Figures 7(a-d) show the liquid fraction (β) fields at time t = 50 min for W_f = 20 mm and 48 mm and area fractions of ϕ = 0.01, 0.05, 0.2 and 0.3, respectively. In the figures, the first and third columns present β fields with respect to the case W_f = 20 mm; similarly, the second and fourth columns are with respect to W_f = 48 mm. As observed in Fig. 7(a-d), there is a reduction of the total time of the melting process for any ϕ with an increase in the fin width W_f, which also corresponds to a reduction in the value of RA_f. In addition, it can be seen that the liquid fraction fields near the right vertical wall are similar to each other for both W_f = 20 mm and W_f = 48 mm, featuring a thin layer of molten PCM for different RA_f and ϕ values. It is also noted that at t = 50 min and for ϕ = 0.01 to 0.05, within different values of RA_f, the solid-liquid interface profiles are similar to each other, differing only in the region to the left of the fin between W_f = 20 mm and W_f = 48 mm.

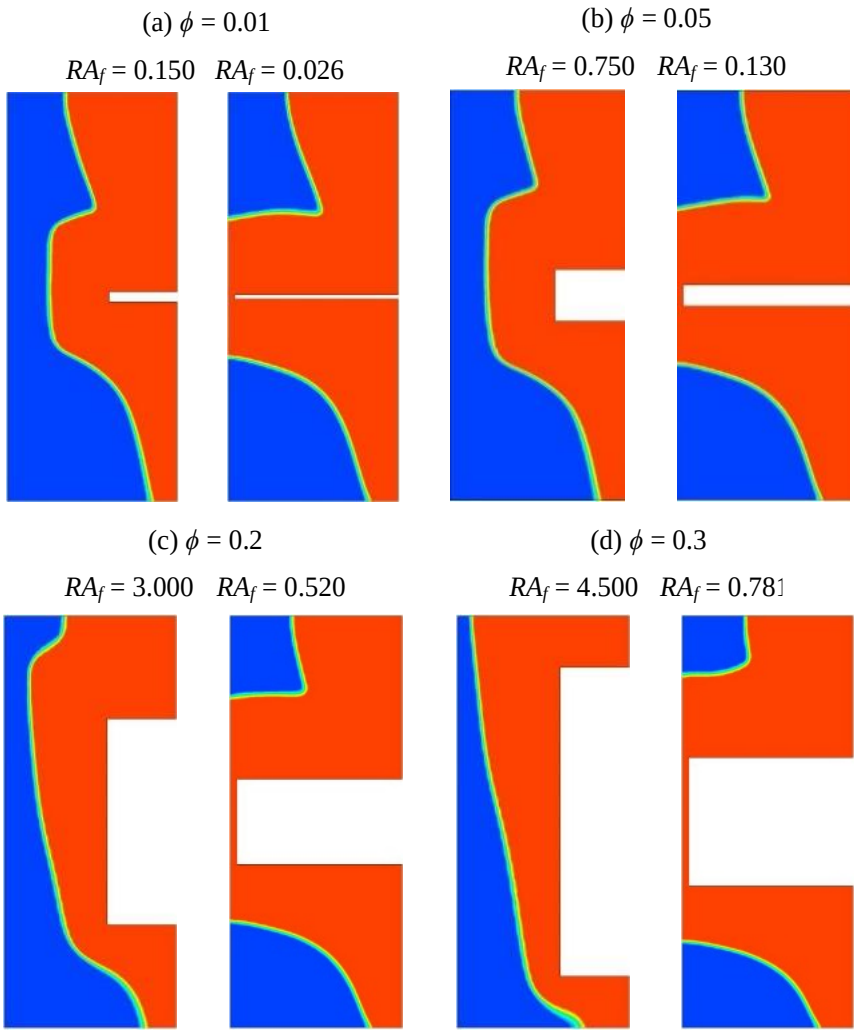

Figure 7 – β field at t = 50 min, W_f = 20 and 48 mm: (a) ϕ = 0.01; (b) ϕ = 0.05; (c) ϕ = 0.2 and (d) ϕ = 0.3.

4.3 Effect of Fin Aspect Ratio (RA_f)

The different heat transfer mechanisms in a melting process can be identified by varying the Nusselt number ($Nu = h\,L_c/k_l$) as a function of Fourier number ($Fo = \alpha_l\,t/L_c^2$), where L_c is the characteristic length ($L_c = A_c^{1/2}$), A_c is the cavity area, h is the heat transfer coefficient ($h = q''/(T_w - T_l)$), q'' is the heat flux on the right sidewall and fin perimeter, T_w (343 K) is the wall temperature, T_l is the PCM liquid temperature and α_l ($\alpha_l = k_l/\rho_l\,c_{p\,l}$) is the liquid thermal diffusivity. The heat flux (q'') was obtained on CFX-Post from the results obtained from Fluent.

Figure 8(a-f) shows *Nu* profiles as a function of *Fo* for different RA_f and ϕ = 0.01, 0.03, 0.05, 0.1, 0.2, and 0.3, respectively. As seen in the figure, regardless of the values of RA_f and ϕ, all results show 3 different regions: I – with a marked reduction of *Nu* in the initial moments; II - with *Nu* values without large variations, despite fluctuations in most of the melting process and III – a sharp reduction of *Nu* in the final moments. More specifically, the low thermal resistance of the thin wall-melted PCM layer in the initial moments allows the characterization of region I as conductive. With the beginning of the melting process, still in region I, there is an increase in the size of the liquid layer. This behavior induces a change in the heat transfer mechanism from conductive to convective represented by region II. In region II, *Nu* continues to decrease but more slowly. This behavior is in accordance with reference work (Ji et al. 2018) and corroborates with the observations on the velocity fields (Fig. 5): heating at the fin tip produces recirculation of the Rayleigh-Bénard liquid PCM which generates, in turn, fluctuations in the local temperature. Consequently, *Nu* also has fluctuations as seen in region II of Fig. 8(a-f). These oscillations decrease as the solid-liquid interface moves away from the fin in accordance with known experimental behavior (Kamkari and Shokouhmand 2014). In addition, regarding Fig. 8(a-f), it can be observed that smaller values of RA_f ($RA_f = H_f / W_f$) are associated with longer periods of *Nu* fluctuations. This behavior is due to the increase of W_f. Moreover, it is observed that increasing the value of ϕ reduces the amplitude of the instabilities, which is visually evident in a comparison of Fig. 8(a) and 8(f). This fact justifies the reduction of the time difference of the melting process with increasing of ϕ seen in the analysis of the liquid fraction profiles. In region III, at the final moments, *Nu* number again decreases more sharply due to the reduction of the heat transfer rate resulting from weakening convection currents. In this figure it can also be observed that, for all values ϕ and near *Fo* = 0.05, there is a small increase in *Nu* for the highest RA_f values. This behavior occurs due to the greater length of the solid-liquid PCM interface, as seen in Fig. 7(a-d). For example, in Fig. 7(a) for ϕ=0.01, the length of the solid-liquid interface for RA_f = 0.15 is greater than for RA_f = 0.026, resulting in a larger *Nu* seen in Fig. 8(a). As a final point, it should be mentioned that for all tested ϕ values, the cases with the lowest *Nu* are those that presented the fastest melting processes.

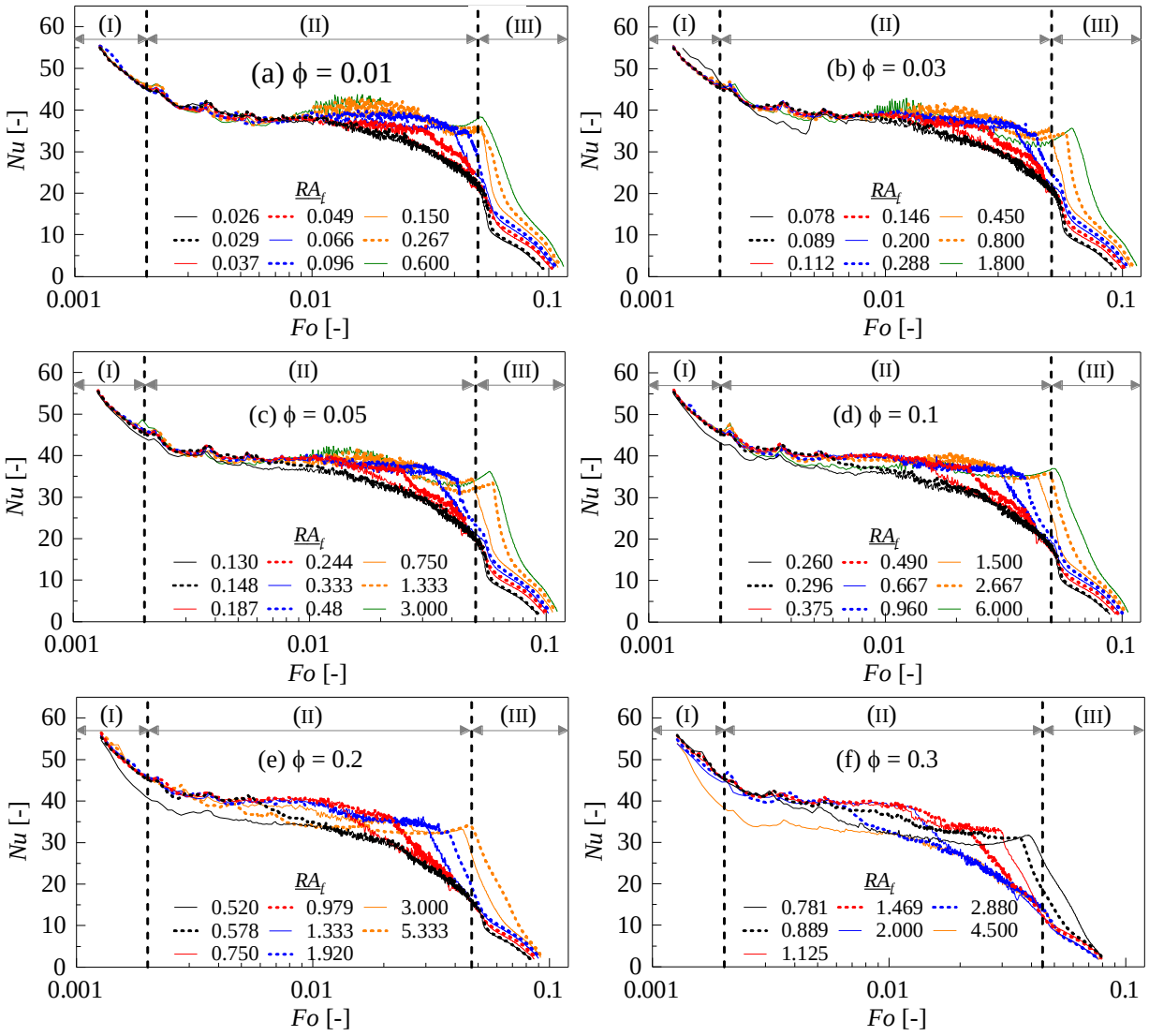

Figure 8 – *Nu* vs. *Fo*, for several values of RA_f and: (a) ϕ = 0.01; (b) ϕ = 0.03; (c) ϕ = 0.05; (d) ϕ = 0.1; (e) ϕ = 0.2 and (f) ϕ = 0.3.

Figures 9(a-c) show β fields for ϕ = 0.005 at times t = 1 min, 10 min, 30 min, 50 min, 70 min and 90 min and RA_f = 0.300, 0.033 and 0.013, respectively. As in Fig. 7, blue color represents the solid phase and red color represents the liquid phase. Initially, it is observed that at t = 1 min, regardless of the values of RA_f, the fused PCM layer in the vicinity of the heated wall is very thin. At this time, the PCM is almost entirely in the solid phase and the heat transfer process is predominantly conductive. As t increases, the thickness of the molten layer increases and buoyant forces become predominant in relation to viscous ones; therefore, a change in the heat transfer mechanism occurs, becoming convective. As a result, solid-phase erosion occurs in the upper cavity at the solid-liquid interface, forming a curvature of the melting front. This can be observed in Fig 9 for all values of RA_f

at t = 30 min, 50 min and 70 min. Additionally, it is noted that RA_f also influences the melting rate. For example, after the initial moments, there is a tendency to accelerate the PCM merger process with reduced RA_f. This is mainly identified at t = 50 min, where it can be observed that the melting rate for RA_f = 0.013 is much larger than for RA_f = 0.3. This behavior is due to the augmented perimeter of the fin inserted in the PCM, which increases the heat transfer area between the fin and the PCM.

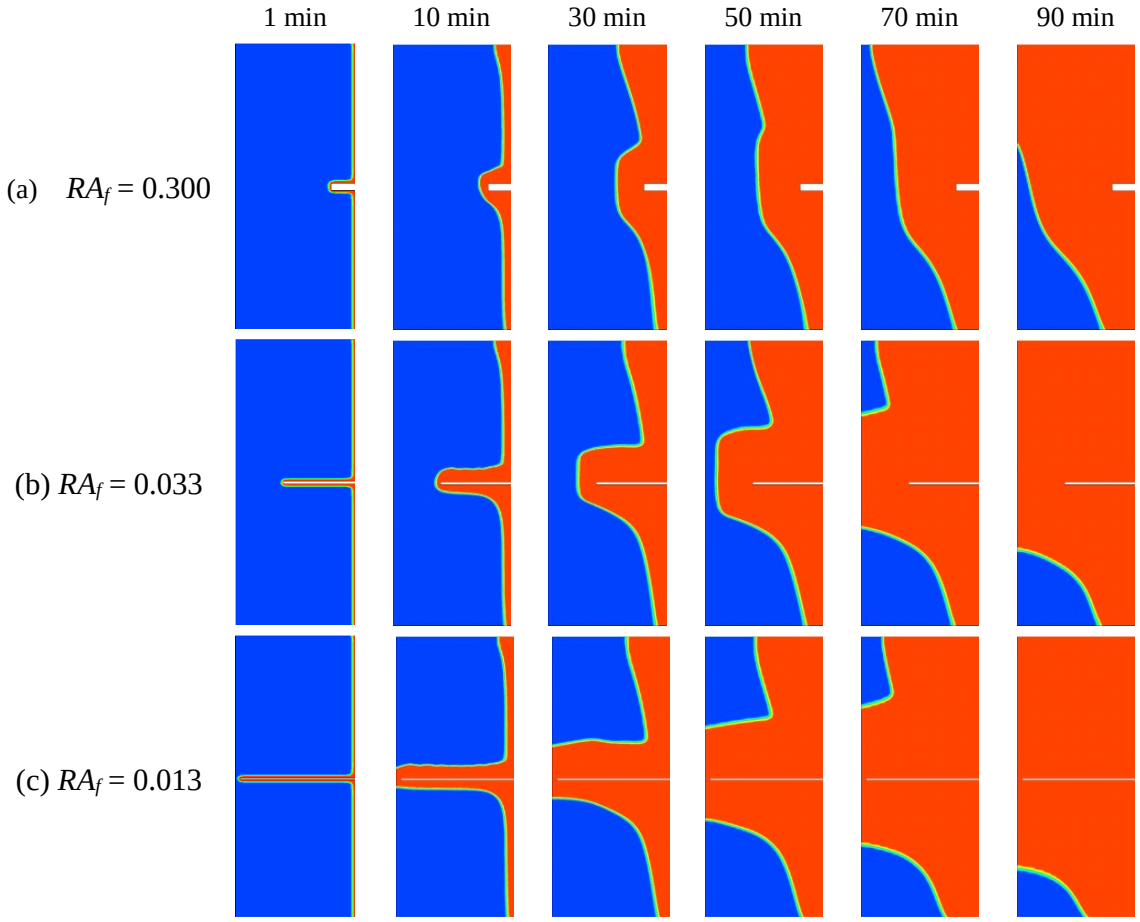

Figure 9 – β field for ϕ = 0.005, t = 1 min, 10 min, 30 min, 50 min, 70 min and 90 min, and: (a) RA_f = 0.300; (b) RA_f = 0.033 and (c) RA_f = 0.013.

In quantitative terms, the influence of RA_f (H_f /W_f) over β is shown in Fig. 10(a-f) which highlights the variations of β as a function of time for different RA_f and ϕ = 0.01, 0.03, 0.05, 0.1, 0.2 and 0.3, respectively. Overall, higher values of RA_f are associated with longer complete PCM melting times (β = 1) independent of the area fraction ϕ. Moreover, since the increase in RA_f leads to fins with smaller heat exchange area, the heat removal (per unit time) process ends up being penalized. Conversely, it can be demonstrated that there is a gradual tendency of acceleration of the melting process with the gradual reduction of the aspect ratio RA_f for all tested values of ϕ, even if it is not evident which were the smallest calculated RA_f values.

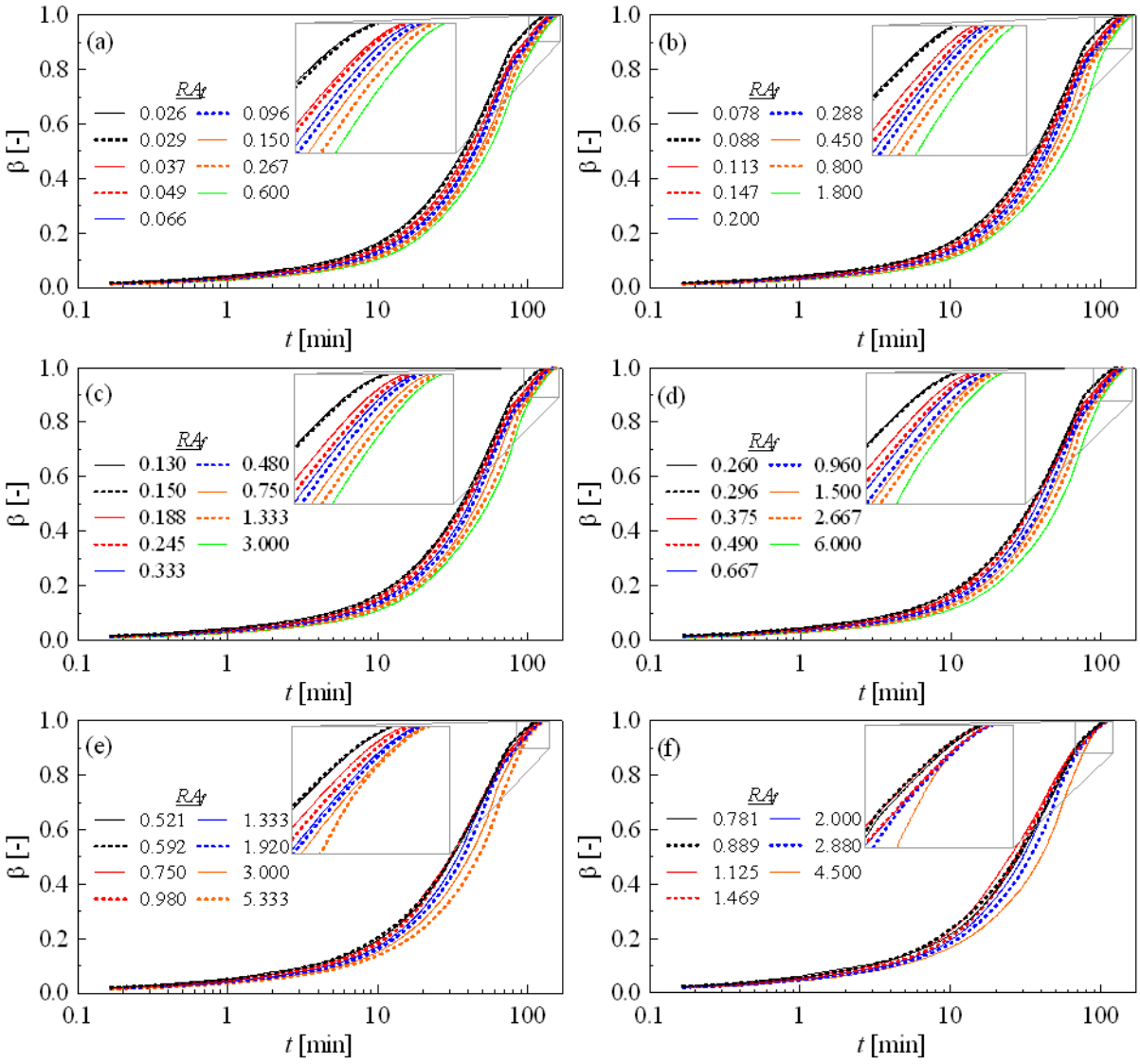

Figure 10 – β vs. t for several values of RA_f and: (a) ϕ = 0.01; (b) ϕ = 0.03; (c) ϕ = 0.05; (d) ϕ = 0.1; (e) ϕ = 0.2 and (f) ϕ = 0.3.

A deeper understanding of how the total melting time is affected by the various parameters can be obtained from Fig. 11: it shows the maximum time of the melting process (β = 1) as a function of RA_f for all the simulated values of ϕ of all 78 configurations. It can be immediately observed that increases of ϕ are associated with decreases in the time required for the PCM to completely melt. For example, at RA_f = 1 and for ϕ = 0.02 and 0.2, the maximum melting times were approximately 165 min and 127 min, respectively. Therefore, the increase of an order of magnitude in the ϕ value led to a reduction of approximately 38 min in the melting process.

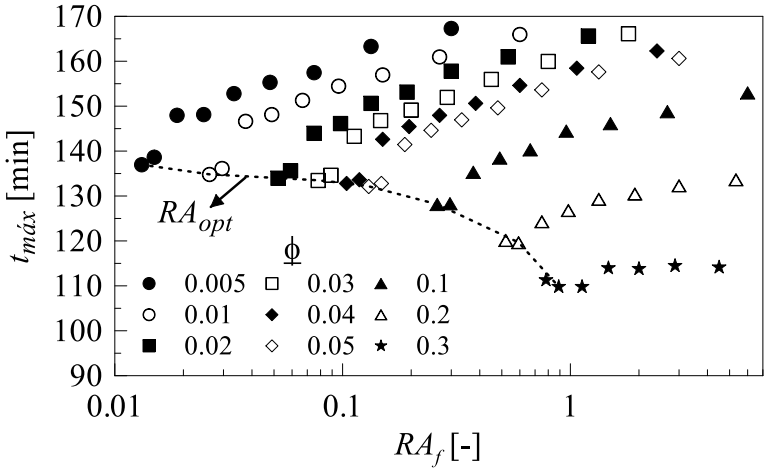

Figure 11 – Maximum melting time of each fin configuration as function of RA_f and several values of ϕ.

For this study the optimum aspect ratio (RA_{opt}) was defined as the one with the lowest melting rate, i.e. the shortest time to reach complete melting for each ϕ. For ϕ ranging from 0.005 to 0.1, the shortest melting times were obtained with the lowest RA_f. However, for ϕ = 0.2 and 0.3, the shortest time occurred in the "second lowest" RA_f, which were designated the proper RA_{opt}. The total trend of the RA_{opt} values is plotted in Figure 12 as a dashed line. Similar behavior was observed for this configuration in other studies (Biserni, Rocha, and Bejan 2004) in which the optimal geometries proved to be the ones which permitted, as far as possible, the morphing "inverted fins" to penetrate the cavity. The optimal values of aspect ratios found in this study are shown in Table 5 with respect to tested values of ϕ.

Table 5 - RA_{opt} at corresponding values of ϕ.

ϕ	0.005	0.01	0.02	0.03	0.04	0.05	0.1	0.2	0.3
RA_{opt}	0.013	0.026	0.052	0.078	0.104	0.130	0.260	0.592	0.889

Further work was conducted with the investigation of the absorbed energy. Since the cavity area (A_c) was constant, the fin area (A_f) obviously increased with increases of the area fraction ($\phi = A_f/A_c$). Under these conditions, increasing ϕ implied a reduction in the amount of mass contained in the cavity and the resulting variation in the energy absorbed by it. This behavior can be observed in Fig. 12, which shows the total energy absorbed by the cavity as a function of time for the optimal aspect ratios RA_{opt} with respect to all tested area fractions ϕ. It can be noticed that, as ϕ increases, there is a reduction in absorbed energy as predicted. For example, between ϕ = 0.1 and ϕ = 0.3 at t = 100 min, the energy absorbed is approximately 861 kJ and 690 kJ, respectively. This represents a reduction of around 20% in terms of absorbed energy. However, for a variation of 10% in area fraction

(ϕ = 0.005 and ϕ = 0.05) at t = 100 min, the absorbed energy is around 935 kJ and 902 kJ, respectively. These values represent a decrease of only approximately 3% of absorbed energy. Based on these results, it can be concluded that the reduction of the absorbed energy should be significant only for values of ϕ greater than a threshold value of 0.05.

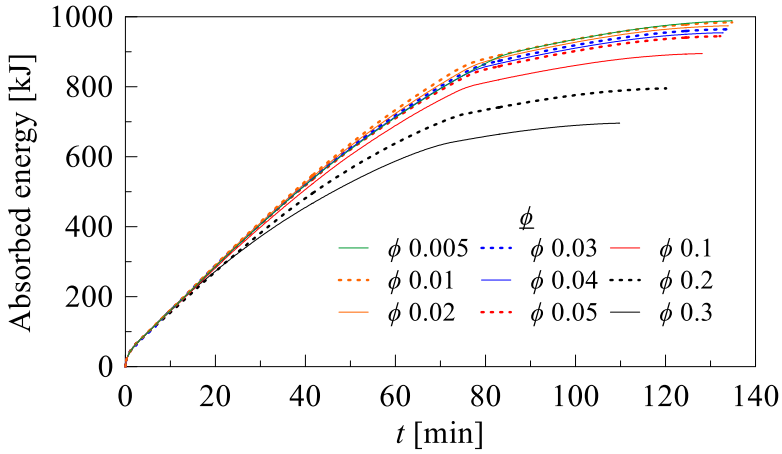

Figure 12 – Cavity absorbed energy over time with respect to the optimal aspect ratios, RA_{opt} and several ϕ values.

Finally, Fig. 13 shows the variation of the energy absorbed in the cavity as a function of time with respect to the cases RA_f = 1.33 and ϕ = 0.05 and 0.2. Figure 13 shows a clear inversion in trend at a time of approximately 80 min. For times shorter than 80 min, an increase in ϕ results in an increase in absorbed energy. For example, at t = 60 min and ϕ = 0.05 and ϕ = 0.2, approximately 549 kJ and 625 kJ were absorbed, respectively. This represents an increase of 12% in absorbed energy when ϕ is increased from 0.05 to 0.2. This behavior may be of great interest in applications that require a high storage rate in shorter times. In contrast, for times longer than 80 min, the opposite behavior is observed with a decrease in ϕ resulting in an increase in absorbed energy. For example, at t = 120 min, for ϕ = 0.05 and 0.2, approximately 890 kJ and 790 kJ were absorbed, respectively. This demonstrates that a 15% increase in area fraction resulted in approximately an 11% reduction in total energy absorption.

Figure 13 – Absorbed energy over time for RA_f = 1.33 and ϕ = 0.05 and 0.2.

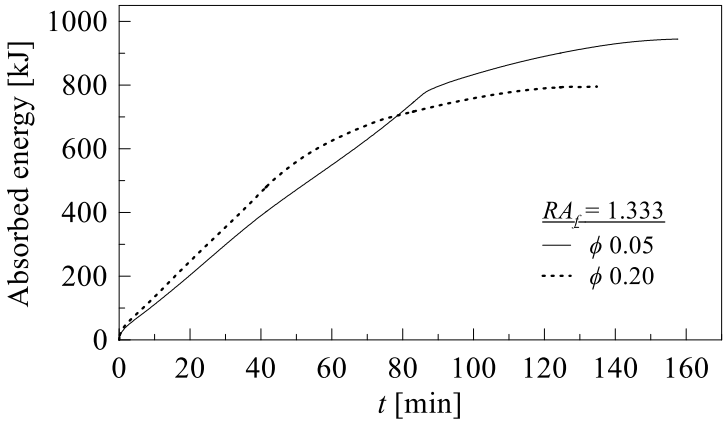

5. Conclusions

The present work was concerned with the effect of the aspect ratio of an "inverted fin", i.e. an intrusion placed in a rectangular cavity, in the melting process of lauric acid PCM. Results were obtained by means of a computational model based on the equations of conservation of mass, momentum, energy and an enthalpy-porosity model representing the PCM melting process. The main conclusions were:

- a shear region between two convective currents was observed. This was a result of a buoyant upward flow in the region above the fin and a downward flow at the solid-liquid interface. Another region with great recirculation was observed between the base of the cavity and the base of the fin. In addition, the existing circulation along the top of the fin was classified as Rayleigh-Bénard convection.
- for all tested values of area fraction (ϕ), there was a reduction in total time of the melting process with a reduction of the value of the fin aspect ratio RA_f, caused by the increase of the fin width W_f. It was also noted that at t = 50 min for ϕ ranging from 0.01 to 0.05, with different values of RA_f, the solid-liquid interface profiles were similar to each other, differing only in the region to the left of the fin between W_f = 20 mm and W_f = 48 mm.
- *Nu* profiles as a function of *Fo* for different RA_f and ϕ = 0.01, 0.03, 0.05, 0.1, 0.2 and 0.3 showed 3 distinct regions. Region I presented a marked reduction of *Nu* in the initial moments (mostly due to conduction). Region II presented *Nu* values without large variations but with fluctuations in most of the melting process (mostly due to convection). Region III presented sharp reductions of *Nu* in the final moments, due to the weakening of convection currents.
- The various parameters affecting the total melting time were investigated with reference to the 78 simulated configurations. The increase of ϕ was associated with decreasing times required

for the PCM to completely melt. For example, for RA_f = 1 and ϕ = 0.02 and 0.2, the maximum melting times were approximately 165 min and 127 min, respectively. Therefore, the increase of an order of magnitude in the value of ϕ led to a reduction of approximately 38 min in the melting process.

- Finally, an investigation regarding the amount of absorbed energy with respect to RA_{opt} was carried out. It was noticed that there was a reduction in absorbed energy as ϕ increased. For example, at t = 100 min for ϕ = 0.1 and ϕ = 0.3, the energy absorbed was approximately 861 kJ and 690 kJ, respectively. This represented a reduction of around 20% in terms of absorbed energy. However, for an increase of 10% of area fraction (ϕ = 0.005 to ϕ = 0.05) at t = 100 min, the absorbed energy was around 935 kJ and 902 kJ, respectively. These values represented a decrease of 3% of absorbed energy. With these results, it was concluded that the reduction of the absorbed energy was significant only for ϕ greater than a threshold value of 0.05.

Acknowledgments

This work was supported by UNISINOS (University of Vale do Rio dos Sinos), CAPES (Coordination for the Improvement of Higher Education Personnel) and FAPERGS (Research Support Foundation of the State of Rio Grande do Sul). Financial support was provided by CAPES (Coordination for the Improvement of Higher Education Personnel) – Grant Financing Code 001. Author C. Biserni was sponsored by the Italian Ministry for Education, University and Research.

References

Abdulateef, Ammar M., Sohif Mat, Kamaruzzaman Sopian, Jasim Abdulateef, and Ali A. Gitan. 2017. "Experimental and Computational Study of Melting Phase-Change Material in a Triplex Tube Heat Exchanger with Longitudinal/Triangular Fins." *Solar Energy* 155: 142–53. https://doi.org/10.1016/j.solener.2017.06.024.

Agyenim, Francis, Neil Hewitt, Philip Eames, and Mervyn Smyth. 2010. "A Review of Materials, Heat Transfer and Phase Change Problem Formulation for Latent Heat Thermal Energy Storage Systems (LHTESS)." *Renewable and Sustainable Energy Reviews* 14 (2): 615–28. https://doi.org/10.1016/j.rser.2009.10.015.

Akeiber, Hussein, Payam Nejat, Muhd Zaimi Abd Majid, Mazlan A. Wahid, Fatemeh Jomehzadeh, Iman Zeynali Famileh, John Kaiser Calautit, Ben Richard Hughes, and Sheikh Ahmad Zaki. 2016. "A Review on Phase Change Material (PCM) for Sustainable Passive Cooling in Building Envelopes." *Renewable and Sustainable Energy Reviews* 60: 1470–97. https://doi.org/10.1016/j.rser.2016.03.036.

Arshad, Adeel, Mark Jabbal, Pouyan Talebizadeh Sardari, Muhammad Anser Bashir, Hamza Faraji, and

538 Yuying Yan. 2020. “Transient Simulation of Finned Heat Sinks Embedded with PCM for Electronics
539 Cooling.” *Thermal Science and Engineering Progress* 18 (August).
540 https://doi.org/10.1016/j.tsep.2020.100520.
541 Aslfattahi, Navid, R. Saidur, Mohd Faizul Mohd Sabri, and A. Arifutzzaman. 2019. "Experimental
542 Investigation of Thermal Stability and Enthalpy of Eutectic Alkali Metal Solar Dispersed with MGO
543 Nanoparticles." *International Journal of Technology* 10 (6): 1112-1119.
544 https://dx.doi.org/10.14716/ijtech.v10i6.3568.
545 Aslfattahi, Navid, R. Saidur, A. Arifutzzaman, R. Sadri, Nuno Bimbo, Mohd Faizul Mohd Sabri, Philip A
546 Maughan, Luc Bouscarrat, Richard J. Dawson, Suhana Mohd Said, Boon Tong Goh, and Nor Azwadi
547 Che Sidik. 2020. "Experimental investigation of energy storage properties and thermal conductivity of
548 a novel organic phase change material/MXene as A new class of nanocomposites." *Journal of Energy*
549 *Storage* 27: 101115. https://doi.org/10.1016/j.est.2019.101115.
550 Baby, Rajesh, and C. Balaji. 2012. “Experimental Investigations on Phase Change Material Based Finned
551 Heat Sinks for Electronic Equipment Cooling.” *International Journal of Heat and Mass Transfer* 55
552 (5–6): 1642–49. https://doi.org/10.1016/j.ijheatmasstransfer.2011.11.020.
553 Biserni, C., L. A.O. Rocha, and A. Bejan. 2004. “Inverted Fins: Geometric Optimization of the Intrusion into
554 a Conducting Wall.” *International Journal of Heat and Mass Transfer* 47 (12–13): 2577–86.
555 https://doi.org/10.1016/j.ijheatmasstransfer.2003.12.018.
556 Celik, Ismail B., Urmila Ghia, Patrick J. Roache, Christopher J. Freitas, Hugh Coleman, and Peter E. Raad.
557 2008. “Procedure for Estimation and Reporting of Uncertainty Due to Discretization in CFD
558 Applications.” *Journal of Fluids Engineering, Transactions of the ASME* 130 (7): 0780011–14.
559 https://doi.org/10.1115/1.2960953.
560 Chuah, T.G., D. Rozanna, A. Salmiah, S. Y. Thomas Choong, and M. Sa’ari. 2006. “Fatty Acids Used as
561 Phase Change Materials (PCMs) for Thermal Energy Storage in Building Material Applications.”
562 *Applied Energy*, no. July: 123–37.
563 Dabiri, Soroush, Mehdi Mehrpooya, and Erfan Ghavami Nezhad. 2018. “Latent and Sensible Heat Analysis
564 of PCM Incorporated in a Brick for Cold and Hot Climatic Conditions, Utilizing Computational Fluid
565 Dynamics.” *Energy* 159: 160–71. https://doi.org/10.1016/j.energy.2018.06.074.
566 Ehms, José Henrique Nazzi, Rejane De Césaro Oliveski, Luiz Alberto Oliveira Rocha, Cesare Biserni, and
567 Massimo Garai. 2019. "Fixed Grid Numerical Models for Solidification and Melting of Phase Change
568 Materials (PCMs)." *Applied Sciences* 9: 4334. https://doi.org/10.3390/app9204334.
569 Hasnain, S M. 1998. “Review on Sustainable Thermal Energy Storage Technologies, Part I: Heat Storage
570 Materials and Techniques.” *Energy Conversion and Management* 39 (11): 1127–38.
571 Ibrahim, Nasiru I., Fahad A. Al-Sulaiman, Saidur Rahman, Bekir S. Yilbas, and Ahmet Z. Sahin. 2017.
572 “Heat Transfer Enhancement of Phase Change Materials for Thermal Energy Storage Applications: A
573 Critical Review.” *Renewable and Sustainable Energy Reviews* 74: 26–50.

https://doi.org/10.1016/j.rser.2017.01.169.
Jaguemont, Joris, Noshin Omar, Peter Van den Bossche, and Joeri Mierlo. 2018. “Phase-Change Materials (PCM) for Automotive Applications: A Review.” *Applied Thermal Engineering* 132: 308–20. https://doi.org/10.1016/j.applthermaleng.2017.12.097.
Jamil, Nurfatihah, Jesbains Kaur, Ak. Pandey, Syed Shahabuddin, Samir Hassani, Rahman Saidur, Roshafima Rasit Ali, Nor Azwadi Che Sidik, and Mohd Naim. 2019. "A Review on Nano Enhanced Phase Change Materials: An Enhancement in Thermal Properties and Specific Heat Capacity."*Journal of Advanced Research in Fluid Mechanics and Thermal Sciences* 57: 110-120.
Ji, Chenzhen, Zhen Qin, Swapnil Dubey, Fook Hoong Choo, and Fei Duan. 2018. “Simulation on PCM Melting Enhancement with Double-Fin Length Arrangements in a Rectangular Enclosure Induced by Natural Convection.” *International Journal of Heat and Mass Transfer* 127: 255–65. https://doi.org/10.1016/j.ijheatmasstransfer.2018.07.118.
Joshi, Varun, and Manish K. Rathod. 2019. “Constructal Enhancement of Thermal Transport in Latent Heat Storage Systems Assisted with Fins.” *International Journal of Thermal Sciences* 145 (November). https://doi.org/10.1016/j.ijthermalsci.2019.105984.
Kalbasi, Rasool, and Mohammad Reza Salimpour. 2015. “Constructal Design of Horizontal Fins to Improve the Performance of Phase Change Material Rectangular Enclosures.” *Applied Thermal Engineering* 91: 234–44. https://doi.org/10.1016/j.applthermaleng.2015.08.024.
Kalnaes, Simen Edsjo, Bjorn Petter Jelle. 2015. "Phase change materials and products for building applications: A state-of-the-art review and future research opportunities." *Energy and Buildings* 94: 150-176. https://dx.doi.org/10.1016/j.enbuild.2015.02.023.
Kamkari, Babak, and Hossein Shokouhmand. 2014. “Experimental Investigation of Phase Change Material Melting in Rectangular Enclosures with Horizontal Partial Fins.” *International Journal of Heat and Mass Transfer* 78: 839–51. https://doi.org/10.1016/j.ijheatmasstransfer.2014.07.056.
Kazemi, M., M. J. Hosseini, A. A. Ranjbar, and R. Bahrampoury. 2018. “Improvement of Longitudinal Fins Configuration in Latent Heat Storage Systems.” *Renewable Energy* 116: 447–57. https://doi.org/10.1016/j.renene.2017.10.006.
Khan, Mohammed Mumtaz A., R. Saidur, Fahad A. Al-Sulaiman. 2017. "A review for phase change materials (PCMs) in solar absorption refrigeration systems." *Renewable and Sustainable Energy Reviews* 76: 105-137. https://doi.org/10.1016/j.rser.2017.03.070.
Kok, Besir. 2020. “Examining Effects of Special Heat Transfer Fins Designed for the Melting Process of PCM and Nano-PCM.” *Applied Thermal Engineering* 170 (April). https://doi.org/10.1016/j.applthermaleng.2020.114989.
Leducq, D., F. T. NDoye, G. Alvarez. 2015. "Phase change material for the thermal protection of ice cream during storage and transportation." *International Journal of Refrigeration* 52: 133-139. http://dx.doi.org/10.1016/j.ijrefrig.2014.08.012.

Mostafavi, Amirhossein, Mohammad Parhizi, and Ankur Jain. 2019. “Theoretical Modeling and Optimization of Fin-Based Enhancement of Heat Transfer into a Phase Change Material.” *International Journal of Heat and Mass Transfer* 145 (December). https://doi.org/10.1016/j.ijheatmasstransfer.2019.118698.

Pielichowska, Kinga, and Krzysztof Pielichowski. 2014. “Phase Change Materials for Thermal Energy Storage.” *Progress in Materials Science* 65: 67–123. https://doi.org/10.1016/j.pmatsci.2014.03.005.

Pizzolato, Alberto, Ashesh Sharma, Kurt Maute, Adriano Sciacovelli, and Vittorio Verda. 2017. “Design of Effective Fins for Fast PCM Melting and Solidification in Shell-and-Tube Latent Heat Thermal Energy Storage through Topology Optimization.” *Applied Energy* 208 (October): 210–27. https://doi.org/10.1016/j.apenergy.2017.10.050.

Pu, Liang, Shengqi Zhang, Lingling Xu, and Yanzhong Li. 2020. “Thermal Performance Optimization and Evaluation of a Radial Finned Shell-and-Tube Latent Heat Thermal Energy Storage Unit.” *Applied Thermal Engineering* 166 (November 2019): 114753. https://doi.org/10.1016/j.applthermaleng.2019.114753.

Reddy, K. S., Vijay Mudgal, and T. K. Mallick. 2018. “Review of Latent Heat Thermal Energy Storage for Improved Material Stability and Effective Load Management.” *Journal of Energy Storage* 15: 205–27. https://doi.org/10.1016/j.est.2017.11.005.

Shokouhmand, Hossein, and Babak Kamkari. 2013. “Experimental Investigation on Melting Heat Transfer Characteristics of Lauric Acid in a Rectangular Thermal Storage Unit.” *Experimental Thermal and Fluid Science* 50: 201–12. https://doi.org/10.1016/j.expthermflusci.2013.06.010.

Souayfane, Farah, Farouk Fardoun, Pascal-Henry Biwole. 2016. "Phase change materials (PCM) for cooling applications in buildings: A review."*Energy and Buildings* 129: 396-431. http://dx.doi.org/10.1016/j.enbuild.2016.04.006.

Sun, Kun, Huan Liu, Xiaodong Wang, and Dezhen Wu. 2019. “Innovative Design of Superhydrophobic Thermal Energy-Storage Materials by Microencapsulation of n-Docosane with Nanostructured ZnO/SiO2 Shell.” *Applied Energy* 237 (January): 549–65. https://doi.org/10.1016/j.apenergy.2019.01.043.

Valeri, Daniella, and Antonio J.A. Meirelles. 1997. “Viscosities of Fatty Acids, Triglycerides, and Their Binary Mixtures.” *JAOCS, Journal of the American Oil Chemists’ Society* 74 (10): 1221–26. https://doi.org/10.1007/s11746-997-0048-6.

Voller, V. R., and C. Prakash. 1987. “A Fixed Grid Numerical Modelling Methodology for Convection-Diffusion Mushy Region Phase-Change Problems.” *International Journal of Heat and Mass Transfer* 30 (8): 1709–19. https://doi.org/10.1016/0017-9310(87)90317-6.

Wu, Shaofei, Ting Yan, Zihan Kuai, and Weiguo Pan. 2020. “Thermal Conductivity Enhancement on Phase Change Materials for Thermal Energy Storage: A Review.” *Energy Storage Materials* 25 (September 2019): 251–95. https://doi.org/10.1016/j.ensm.2019.10.010.

Zhang, Huili, Jan Baeyens, Gustavo Cáceres, Jan Degrève, and Yongqin Lv. 2016. “Thermal Energy Storage: Recent Developments and Practical Aspects.” *Progress in Energy and Combustion Science* 53: 1–40. https://doi.org/10.1016/j.pecs.2015.10.003.

Zhang, Xuelai, Xudong Chen, Zhong Han, and Weiwen Xu. 2016. “Study on Phase Change Interface for Erythritol with Nano-Copper in Spherical Container during Heat Transport.” *International Journal of Heat and Mass Transfer* 92: 490–96. https://doi.org/10.1016/j.ijheatmasstransfer.2015.08.095.

Zhu, Na, Zhenjun Ma, and Shengwei Wang. 2009. “Dynamic Characteristics and Energy Performance of Buildings Using Phase Change Materials: A Review.” *Energy Conversion and Management* 50 (12): 3169–81. https://doi.org/10.1016/j.enconman.2009.08.019.